

RESEARCH ARTICLE

Markov random field model for segmenting large populations of lipid vesicles from micrographs

Jernej Zupanc¹, Damjana Drobne², Branko Ster¹

¹Faculty of Computer and Information Science, University of Ljubljana, Trzaska 25, SI-1000 Ljubljana, Slovenia, and

²Biotechnical Faculty, Department of Biology, University of Ljubljana, Jamnikarjeva 101, SI-1000 Ljubljana, Slovenia

Abstract

Giant unilamellar lipid vesicles, artificial replacements for cell membranes, are a promising tool for in vitro assessment of interactions between products of nanotechnologies and biological membranes. However, the effect of nanoparticles can not be derived from observations on a single specimen, vesicle populations should be observed instead. We propose an adaptation of the Markov random field image segmentation model which allows detection and segmentation of numerous vesicles in micrographs. The reliability of this model with different lighting, blur, and noise characteristics of micrographs is examined and discussed. Moreover, the automatic segmentation is tested on micrographs with thousands of vesicles and the result is compared to that of manual segmentation. The segmentation step presented is part of a methodology we are developing for bio-nano interaction assessment studies on lipid vesicles.

Keywords: Image processing, image segmentation, markov random field, lipid vesicle, nanoparticles, cell segmentation

1 Introduction

In this paper, we present an adaptation of the Markov random field image segmentation model for extraction of giant unilamellar lipid vesicle shapes from micrographs.

Artificial lipid vesicles, including giant unilamellar lipid vesicles (vesicles) offer a simple biological system with which to study interactions between nanoparticles and biological membranes (Drobne et al., 2009; Zupanc et al., 2010a; Barauskas et al., 2010). Transformations of the shapes of vesicles are frequently used as parameters in research on the interactions between lipid membranes and various agents. Different authors report that in the presence of agents or if external conditions such as temperature or osmotic pressure are varied, vesicles undergo distinct shape changes from one class of shapes to another (Hong et al., 2006; Peterlin et al., 2009). It was shown that nanoparticles also interact strongly with cell membranes (Imparato et al., 2005; Liu et al., 2008; Valant et al., 2009) and that vesicle morphological transformations can also be affected by nanoparticles (Zupanc et al., 2010a).

In studies on the transformation of the shapes of lipid vesicles, vesicles are most often observed singly (Pecreaux et al., 2004; Gruhn et al., 2007; Leirer et al., 2009). In such studies one vesicle is chosen and isolated, and its morphological behavior is recorded. To extend this research, we proposed a population-based approach, in which thousands of vesicles are recorded (Zupanc et al., 2010a) and their morphological changes are analyzed. Because manual segmentation of such a large GUV quantity is extremely time consuming we developed an automated segmentation approach. To segment the vesicles, we selected a Markov random field model (MRF), a frequently applied model in image interpretation processes (Li, 2009). In MRF, classification of a particular pixel in the image is based on the classification of neighboring pixels rather than on the pixel intensity alone. For example, to segment the image into two classes, foreground and background, an MRF model for spatial interaction between pixels will cause the pixels with neighbors classified as foreground also to be classified as foreground with greater probability. This exploitation of a priori

Address for Correspondence:

(Received 09 November 2010; revised 23 February 2011; accepted 08 March 2011)

models of spatial interaction between image pixels can compensate for deficiencies in observed information, and is also applicable in the case of vesicle segmentation from micrographs. Our adaptation of the MRF model is particular for the case of vesicles, as the vesicle halo is used to segment the vesicles with greater accuracy.

The aim of this work was to propose an automated segmentation of multiple vesicles from single micrographs, replacing hours of manual segmentation with seconds of computer processing. We discuss the advantages of this automated segmentation and its applicability to micrographs with various characteristics such as blurred, micrographs with noise, and variable lighting intensity. Moreover, the automatic segmentation is tested on thousands of vesicles and the results are compared to those manually segmented.

2 Lipid vesicle segmentation

2.1 Previous work

A typical vesicle, observed at 400x magnification with a phase contrast light microscope, can be recognized as a dark spherical region, surrounded by a bright halo (Figure 1). When gray level intensities in the two different regions of the vesicle are compared, the following differences can be observed. The darkest regions of the micrographs are the vesicles, the brightest regions are the vesicle halos and both intensity distributions are wider than the intensity distribution of the micrograph background (Figure 2). However, in order to use direct approaches and segment the vesicles by direct intensity thresholding, the intensity distributions should not overlap. In this case, this is not so, and more advanced segmentation approaches are necessary.

In published research, several methods for lipid vesicle segmentation have been proposed. A standard approach is to exploit the high gray level intensity regions of the halo to extract its contour by using an edge detector (Peterlin et al., 2009). Manually selected points within the vesicles have also been used as origins of a polar coordinate system from which a series of radial rays pointing towards the phospholipid membrane are generated. The profiles of image intensities, projected along the rays, contain distinctive patterns that result from the halo effect (Pecreaux et al., 2004; Usenik et al., 2010). Both approaches are adequate for segmenting single vesicles

from micrographs, but fail when multiple vesicles are present. For such cases, we previously proposed a two tier detection system. In the first tier, thresholding and morphological operations are applied to acquire regions where the vesicles are present. In the second tier, a fine vesicle border detection is applied with the usage of the determinant of the Hessian of intensity values at every pixel (Zupanc et al., 2010b). Although this method works well in most cases it fails where intensity of a vesicle varies. In such situations, the algorithm splits a single vesicle into two, each with more homogeneous intensity.

2.2 Markov random field segmentation

In general, image segmentation can be described as assignment of class labels to individual pixels of the image, the goal being to divide the image into distinct regions (Held et al., 1997; Kato et al., 2006; Alomari et al., 2008; Li, 2009). Pixels of each region share some kind of similarity, involving for example, proximity and intensity levels, which must be quantified and incorporated into a model that assigns each pixel to a region. Using the Bayesian approach (Geman et al., 1984), we assume a set of observed (Y) and a set of hidden (X) random variables. The observation $F \in Y$ represents low-level features of the image, in our case grayscale intensity, and the hidden $\phi \in X$ represents the segmentation.

If the probability distribution $P(F|\phi)$ is the imaging model and $P(\phi)$ is a prior distribution, the Bayes theorem gives the posterior distribution $P(\phi|F) \propto P(F|\phi)P(\phi)$. We are interested in ϕ^* which maximizes the posterior estimate of the hidden field X . When the above distributions are functions of certain parameters gathered from the training set, this is called supervised segmentation.

Since many low and high level computer vision problems can be formulated as Bayesian labeling, a MRF modeling approach is very appropriate (Li, 2009). The class of each pixel p is specified by a class label ϕ_p , which is a discrete random variable having values in $\psi = \{1, 2, \dots, T\}$. The set of labels $\phi = \{\phi_p | p \in P\}$ is a random field termed the label process (Kato et al., 2006). The features from the observed image are a realization $F = \{f_p | p \in P\}$ from another random field, which depends on the label process ϕ . The image process F is a sort of manifestation of the label process. We assume that the image process is a noisy version of the underlying label process, which we want to identify. The aim is to find a labeling ϕ^* maximizing the

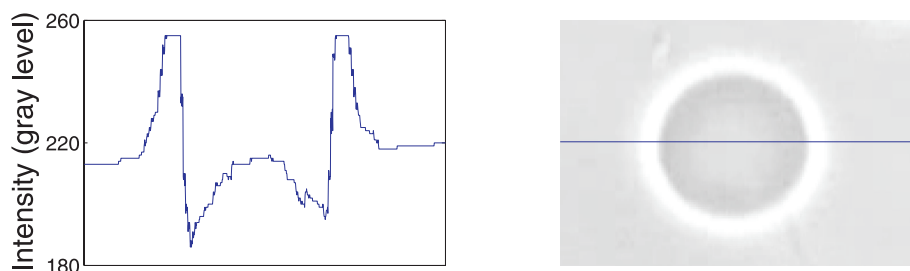


FIGURE 1. A vesicle extracted from a micrograph (right) and an intensity gray level value plot (left) of a cross section of the same vesicle, marked with the horizontal line in the image of the vesicle. On the vertical axis, 0 is the black intensity, and 255 is the white.

posterior probability $P(\phi|F)$, which is the maximum of a posteriori (MAP) estimate:

$$\phi^* = \arg \max_{\phi \in \Phi} P(F|\phi)P(\phi)$$

where ϕ is the set of all possible labelings. The label process ϕ is modeled as a Markov random field. $P(\phi)$ follows the Gibbs distribution

$$P(\phi) = \frac{1}{Z} \exp(-U(\phi)) = \frac{1}{Z} \exp\left(-\sum_{c \in C} V_c(\phi_c)\right)$$

where Z is the normalizing constant and V_c is the clique potential of clique $C \in c$ with the label ϕ_c . C is the set of second order cliques or doubletons, which correspond to pairs of neighboring pixels. The potential must be such that it favors equal classes for neighboring pixels:

$$V_c = \delta(\phi_p, \phi_r) = \begin{cases} +1 & \text{if } \phi_p \neq \phi_r \\ -1 & \text{Otherwise} \end{cases}$$

The complete prior is therefore

$$P(\phi_p) = \frac{1}{Z} \exp\left(-\sum_{\{p,r\} \in C} \delta(\phi_p, \phi_r)\right).$$

In this way, the more homogeneous the segmentation solutions, the higher are their associated probabilities.

We assume that our features (grayscale intensities) f_p for a given class ψ are normally distributed around the mean vector μ_ψ with σ_ψ as standard deviation

$$N(\mu_\psi, \sigma_\psi) = \frac{1}{\sqrt{2\pi\sigma_\psi^2}} \exp\left(-\frac{1}{2} \left(\frac{f - \mu_\psi}{\sigma_\psi}\right)^2\right),$$

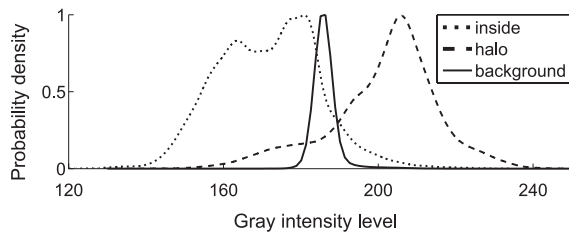


FIGURE 2. The probability density functions of gray level intensities for all three regions - the vesicle, the halo, and the background.

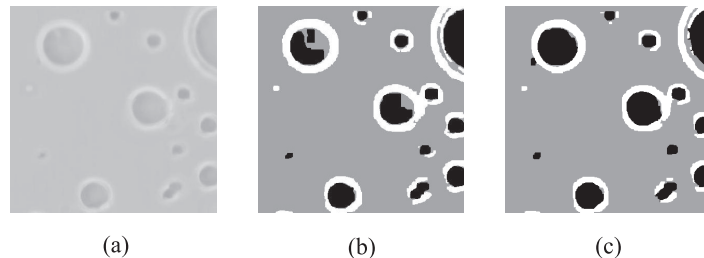


FIGURE 3. (a) Original image, (b) segmented image without correction (MRF), and (c) segmented image with correction (MRF2).

for each pixel class $\psi \in \Psi$. Since the features are assumed to be independent (Kato et al., 2006), the probability is the product

$$P(F|\phi) = \prod_{p \in P} (f_p | \phi_p) = \prod_{p \in P} \frac{1}{\sqrt{2\pi\sigma_{\phi_p}^2}} \exp\left(-\frac{1}{2} \left(\frac{f_p - \mu_{\phi_p}}{\sigma_{\phi_p}}\right)^2\right)$$

The posterior probability $P(\phi|F)$ has two terms: double clique potentials (due to $P(\phi)$) and singleton potentials (due to $P(F|\phi)$). The former models the context of neighboring pixels, while the latter corresponds to modelling the labels without context. $P(\phi|F)$ without the normalizing constant is

$$P(\phi|F) \propto \exp(-U(\phi|F)) \\ \propto \exp\left(-\sum_{p \in P} V_p(\phi_p, f_p) - \beta \sum_{\{p,r\} \in C} \delta(\phi_p, \phi_r)\right)$$

where β is a weight regulating the relevance of the prior, $\beta > 0$. The singleton potentials are

$$V_p(\phi_p, f_p) = \ln \sqrt{2\pi\sigma_{\phi_p}^2} + \frac{1}{2} \left(\frac{f - \mu_{\phi_p}}{\sigma_{\phi_p}}\right)^2.$$

The complete energy function $U(\phi, F)$ is

$$U(\phi, F) = \sum_{p \in P} \left(\ln \sqrt{2\pi\sigma_{\phi_p}^2} + \frac{1}{2} \left(\frac{f - \mu_{\phi_p}}{\sigma_{\phi_p}}\right)^2 \right) + \beta \sum_{\{p,r\} \in C} \delta(\phi_p, \phi_r).$$

The maximum a posteriori estimation corresponds to the following energy minimization

$$\phi^* = \arg \min_{\phi \in \Phi} U(\phi, F)$$

The segmentation problem thus becomes the optimization of the function $U(\phi, F)$. In our case, this was performed with the iterated conditional modes (ICM) algorithm (Besag, 1986).

2.3 Markov random field adjustment for segmenting lipid vesicles

To segment the vesicles, we divide the micrograph pixels into three regions ($T=3$): the vesicle, the halo, and the background. Figure 3a shows a part of the micrograph where multiple vesicles are present before it is segmented. After the micrographs are segmented, the three segmented regions can be observed in Figures 3b

(standard MRF) and Figure 3c (our improved MRF2). As shown in Figure 3b, the MRF segmentation model presented in previous section does not succeed in segmenting the vesicles. Even though the vesicle halo and background regions are segmented correctly, the vesicle inside is classified as background in some cases.

Here we present a correction mechanism for the image segmentation model, allowing a correct segmentation of the vesicles (the result is presented in Figure 3c). This is accomplished by adding an additional potential function (PF) to the function $U(\phi, F)$. The PF is in the following form:

$$PF(\phi, F) = -\gamma \vartheta(\phi_p, 2) \vartheta(\phi_p^-, 1) \rho \left(\sum_{\{p,r\} \in C} \phi_r - \Theta \right)$$

where

$$\vartheta(a, b) = \begin{cases} 1 & \text{if } a=b \\ 0 & \text{Otherwise} \end{cases}$$

and

$$\rho(a) = \begin{cases} a & \text{if } a \geq 0 \\ 0 & \text{Otherwise} \end{cases}$$

The term ϕ_p^- is the previous value of ϕ_p . The complete function to optimize is now $U_2 = U + PF$.

The explanation of the function PF is the following. One would like the background pixels (label 1) which are surrounded by the pixels classified as vesicle (label 2) and the halo pixels (label 3) to be more likely to turn into pixels of the vesicle (label 2). This is the situation where the classification error of the original MRF is the highest (Figure 3b) as the vesicle pixels are falsely classified as the background pixels. Let the label 1 mark the background pixels, 2 the vesicle pixels, and 3 the halo pixels (Table 1).

The function $\vartheta(\phi_p^-, 1)$ reflects the fact that the pixel p was previously marked as background (label 1), and

$\vartheta(\phi_p, 2)$ reflects the fact that the pixel p is now a candidate for the vesicle pixel (label 2). When neighboring pixels of a background pixel have labels 2 and 3, the sum of the label values is high, and when it reaches the predefined threshold Θ , the background pixel turns to a vesicle pixel. The interior of the vesicle is filled in this way completely. The parameter γ is the weighting parameter controlling the importance of the term PF in the context of the complete energy function. The MRF algorithm with this correction mechanism will be denoted as MRF2 in our experiments.

3 Experiments and results

3.1 Vesicle segmentation in synthesized images

First, the proposed MRF2 segmentation is tested on synthesized images of vesicles. These are generated with Matlab and resemble the actual vesicles of sizes 5-20 μm when recorded at 400x magnification with optical microscopy (Figure 4). As an input, both MRF segmentation models require mean values and standard deviations of all regions' gray intensity levels. These are gathered from the vesicle images (Figure 4b) by using the template image (Figure 4a) as a mask to extract intensities of points from a single region. The segmentation of synthesized images is performed to test both, the MRF and MRF2, algorithms segmenting images of different qualities (blurred and noisy). Also, as the images are generated from certain parameters, the ground truth label boundaries are known (Figure 4a) and can be used to assess accuracy of the MRF segmentation compared to the desired result. In order to create different image characteristics, the synthetic image is distorted by first applying a smoothing filter and then adding noise. Smoothing is performed with the Gaussian filter of 7×7 pixels, and noise addition is simulated by adding a random matrix with uniformly distributed values to the image. To obtain results with different image characteristics, the standard deviations for the Gaussian filter are set to $\sigma = 1, 3, 5, 7, 9$, and the noise matrix is multiplied by 0.005, 0.01, 0.02, 0.03, and 0.05. The results from the segmentation of the synthetic

TABLE 1. Labels for background, vesicle, and halo.

label	element	color in segmented images
1	background	gray
2	vesicle	black
3	halo	white

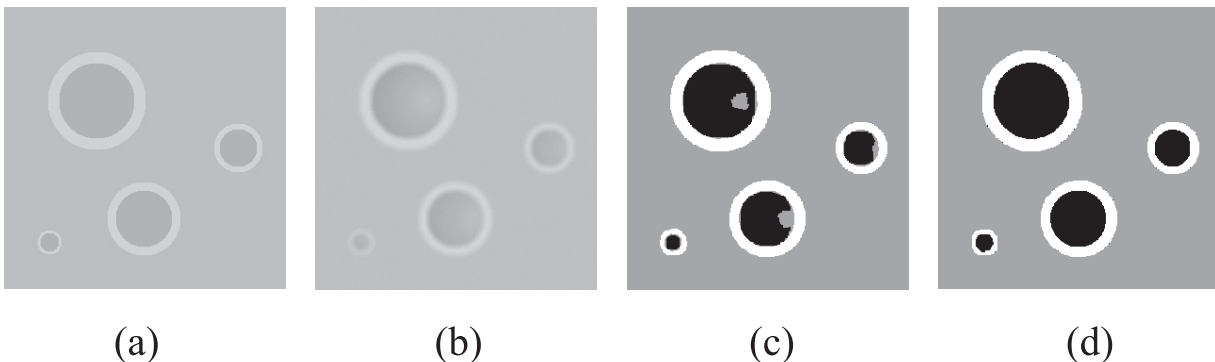


FIGURE 4. (a) The template for synthetic vesicle preparation, (b) synthetic vesicle model, (c) synthetic vesicles segmented with basic MRF (at $\sigma=5$, noise=0.02), and (d) synthetic vesicles segmented with our MRF2.

images with all standard deviations and noise levels are presented in Figure 5b and 5c.

The misclassification rate (segmentation error) is recorded during each iteration of the ICM algorithm and is much lower with MRF2 than with MRF (2% vs. 12%) after 20 iterations (Figure 5a). The percentage reflects how many pixels of each micrograph were correctly segmented as one of the three regions. Figure 5b shows the dependence of the segmentation error on the smoothing parameter σ . With both algorithms, the segmentation error increases with σ , however, the MRF2 method at largest smoothing level ($\sigma=9$) still outperforms the MRF method at the smallest smoothing level ($\sigma=1$). Figure 5c shows how the noise level influences the segmentation accuracy. Even though the MRF accuracy is reduced to a 50% classification error, the proposed MRF2 is not susceptible to increased noise and achieves only 5% error rate in images with the most

noise. Results obtained with the MRF2 segmentation in Figure 3c show that all the vesicles were segmented successfully. The segmentation obtained with the original MRF (Figure 3b) is unsuccessful in filling the insides of the vesicles. The heuristics for MRF2 are set to $\gamma=2$ and $\Theta=6$. These values are optimal and are used for this and all subsequent examples. The parameter β of the energy function U was set to 2 after testing for an appropriate value.

3.2 Vesicle segmentation in micrographs

Next, we manually segmented two micrographs with 15 vesicles (Figure 6) and 10 vesicles (Figure 7), and compared the segmentation accuracy of the MRF and MRF2 algorithms. In both cases, MRF2 provides superior accuracy (1% error compared to 4% error, Figure 8). The mean values and variances of intensity levels for each of the three regions were obtained from multiple manually labeled micrographs

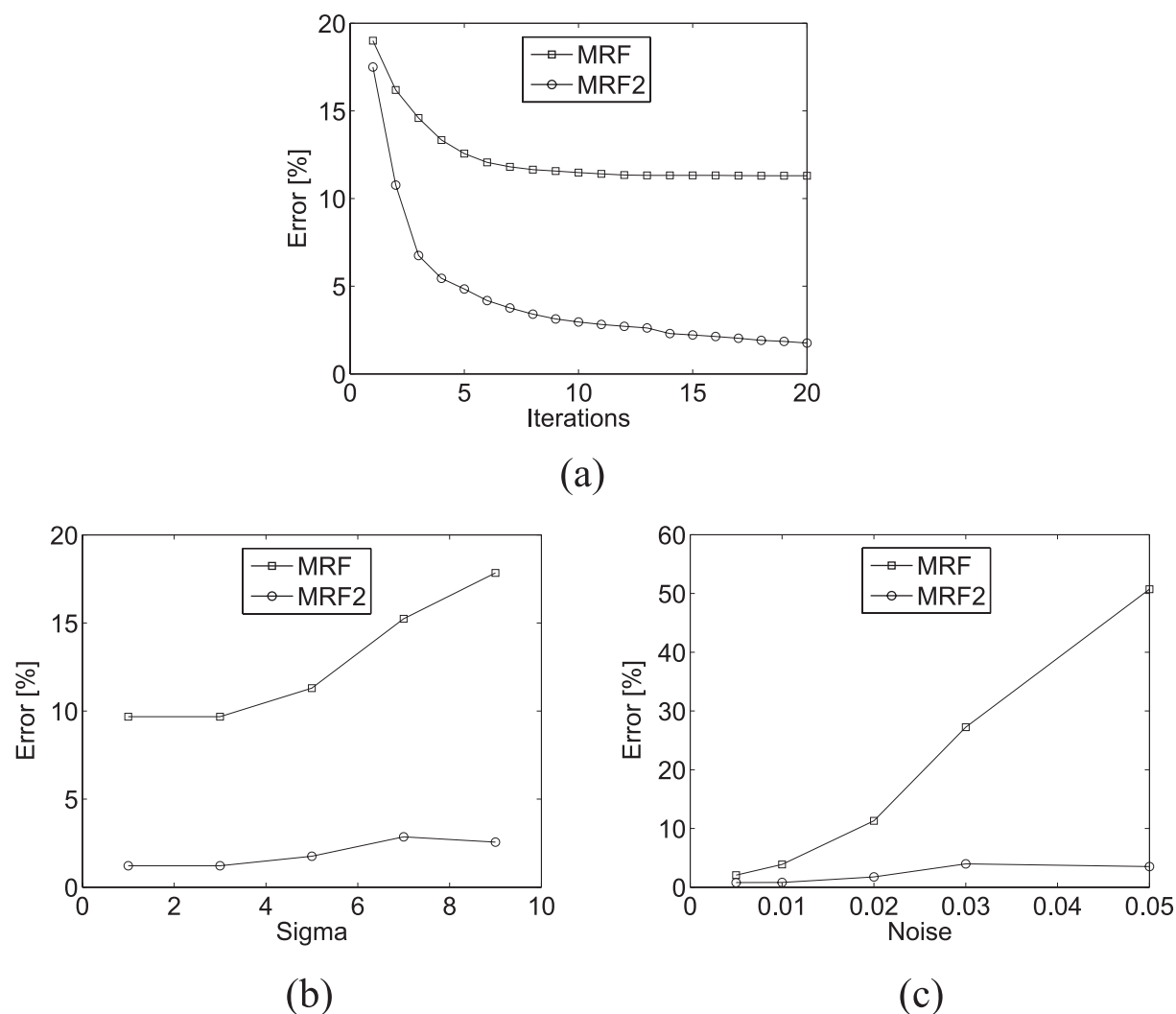


FIGURE 5. (a) Segmentation error of both segmentation models dependent on iterations, (b) segmentation error due to varying smoothing parameter σ , and (c) segmentation error due to varying noise level.

(presented in Figure 2). The main difference that can be observed in both examples is that the MRF2 completely filled the vesicle insides while the MRF algorithm filled them only partially. The results in Figure 8a and 8b show the error rate of each algorithm after each iteration of the ICM algorithm. The MRF2 image segmentation model reached the final accuracy after 7 iterations in both cases while the error rate of the MRF stopped decreasing after 15.

3.3 Segmentation usage in a vesicle population experiment

The main strength of the proposed MRF2 is in segmentation of multiple instead of single vesicles. Such

automatic segmentation finds usage in vesicle population studies (Zupanc et al., 2010a, 2011) where manual segmentation of vesicles is currently most commonly employed. As the quantity of vesicles in these experiments can amount to tens of thousands, manual segmentation is cumbersome and extremely time consuming.

One such experiment was conducted in our previous research (Zupanc et al., 2011), where microscopy video sequences of vesicles incubated in three different suspensions were recorded and each video sequence of an investigated area was stitched into a mosaic, a large image representing the whole area recorded. The

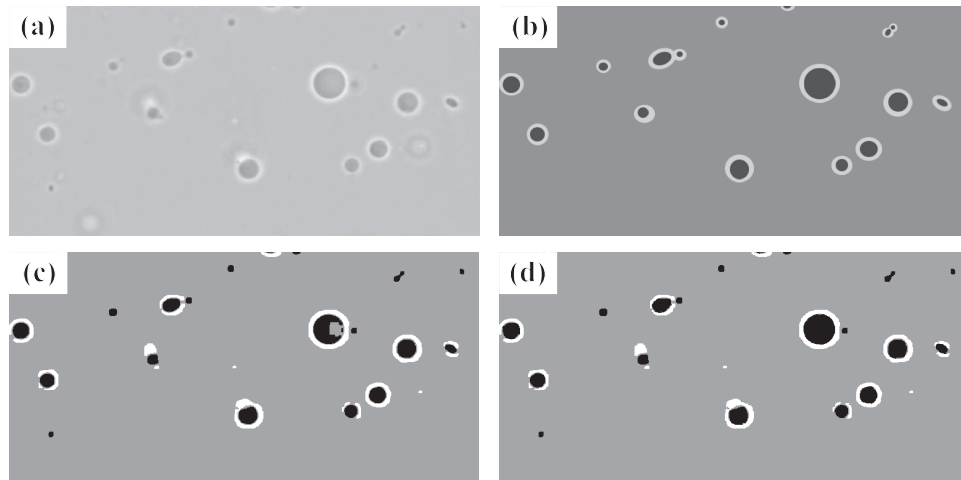


FIGURE 6. (a) Original image of the vesicles, (b) manually segmented image with three classes - background, halo, and vesicle, (c) original image segmented with basic MRF, and (d) original image segmented with our MRF2.

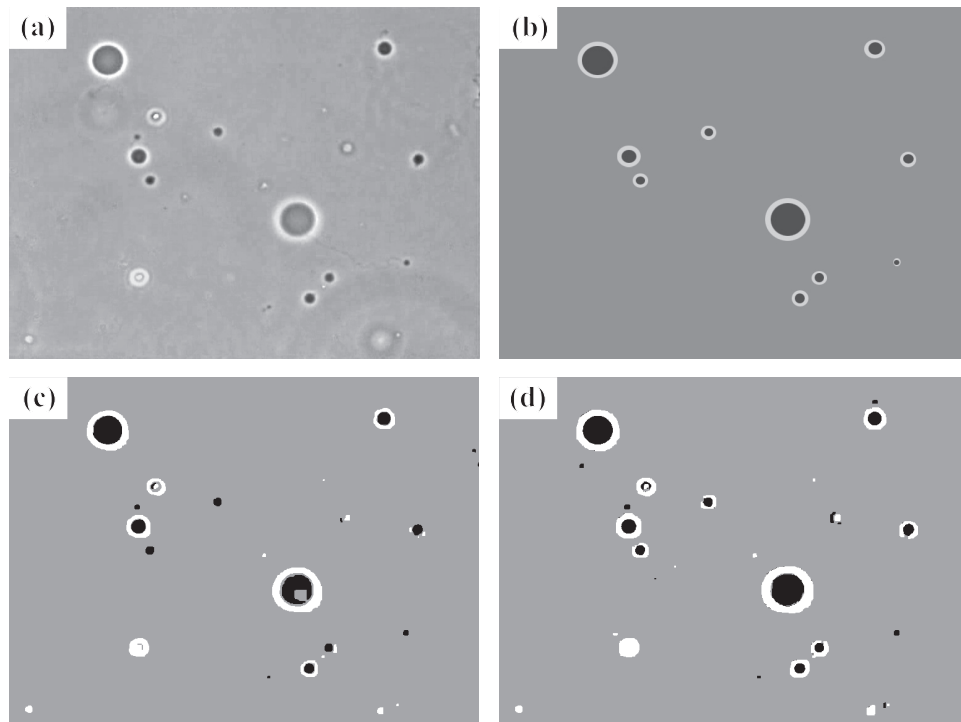


FIGURE 7. (a) Original image of the vesicles, (b) manually segmented image with three classes - background, halo, and vesicle, (c) original image segmented with basic MRF, and (d) original image segmented with our MRF2.

vesicles were then manually segmented from the mosaics and their sizes and shapes were evaluated. In short, the experiment was used to assess the effect of CoFe_2O_4 nanoparticles on the population of vesicles. Three vesicle populations were examined. The first was exposed to neutral CoFe_2O_4 nanoparticles (CF), the second to negatively charged citrate-coated CoFe_2O_4 nanoparticles (CF-CA) and the third population was left unexposed and used as a control (C). The duration of exposure in all three cases was 90 minutes, and the three populations were recorded immediately after exposure and again after 90 minutes.

First, we use the mosaics from the described experiment to test the proposed MRF2 and compare it to the manual segmentation, focusing on the time required and the segmentation accuracy. All together, 6 mosaics were investigated, each containing between 800 and 2200 vesicles. The time required for manual segmentation varied from 5 to 10 hours per mosaic, averaging at 8 hours (Figure 9b). All together, a single experiment (6 mosaics) required 1 week of an operator's labor.

On the other side, the proposed MRF2 algorithm requires almost no human involvement. The algorithm is set to over-segment the mosaic preferring false positives

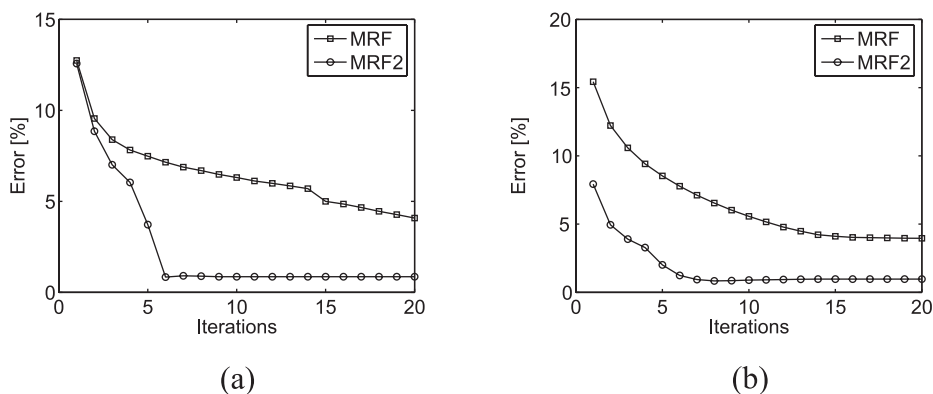


FIGURE 8. Segmentation error of both, MRF and MRF2 algorithms on (a) Figure 6 and (b) Figure 7.

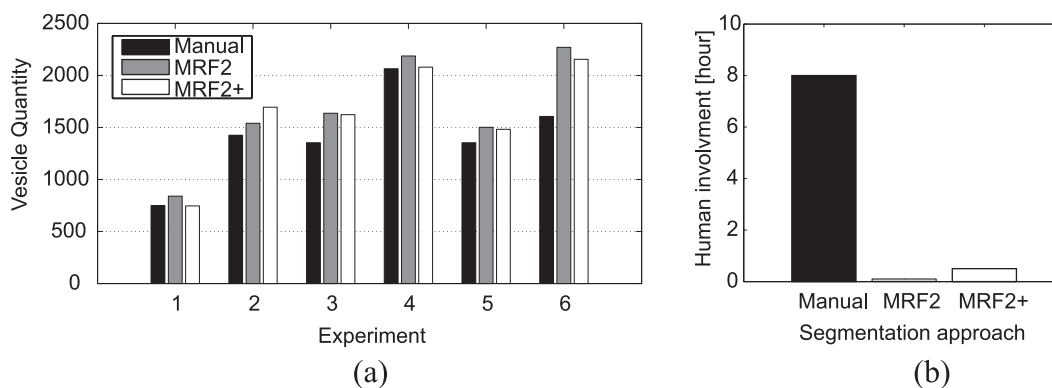


FIGURE 9. (a) The vesicle quantities in each of the six mosaics according to the manually labeled, automatically segmented (MRF2) or automatically segmented with minor corrections by the operator (MRF2+). (b) Hours of the operator's time required for each of the three approaches.

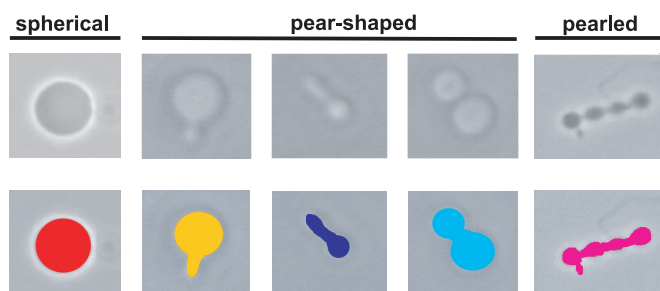


FIGURE 10. A legend representing the observed vesicle types: spherical vesicles (a majority), and nonspherical vesicles, where more specifically the pears (three representatives), and pearls (right) were observed and analyzed. The upper row represents the vesicles as they appear in the micrographs. The bottom row represents the vesicle masks as they appear after being segmented manually or by the MRF2+ algorithm.

over false negatives. After the automatic segmentation, the acquired segmented mosaics are checked by the operator who:

- deletes the false positive vesicle labels,
- adds vesicle labels for vesicles missed by the automatic segmentation,
- identifies nonspherical vesicles and labels them with distinct colors (Figure 10).

This way, one can rely on the results obtained combining MRF2 automatic segmentation with minimal human involvement (MRF2+). Identifying and labeling the nonspherical vesicles (approximately 15% of the population) with distinct colors, allows analyzing the frequencies of their occurrences in the populations. In the case of the CoFe_2O_4 experiment, the two observed nonspherical types of vesicles were the pears and the pearls vesicles (Figure 10).

The vesicle quantity obtained with all three approaches are presented in Figure 9a, where quantities of vesicles detected in each of the 6 mosaics by manual segmentation are compared to the detected quantities by solely MRF2 algorithm or the MRF2 algorithm with the operator's corrections (MRF2+). As expected, the MRF2 over-segmented the mosaics in 5 out of 6 cases. Moreover, the operator's time requirement for corrections was below 1 hour per mosaic on average, allowing completion of the manual labeling of all six mosaics in less time than previously required for a single one. All together, the time required for analyzing data after such experiment was decreased more than eightfold compared to the solely manual segmentation. All mosaics were checked by a second operator afterward and the MRF2+ was

confirmed to be the best approximation of the ground truth. The accuracy of the MRF2+ segmentation also enabled an analysis of spherical vesicle diameter sizes. The mean diameter of the spherical vesicles in the control population (C) decreased from $6.5\ \mu\text{m}$ to $6\ \mu\text{m}$ after 90 minutes of incubation, while the mean diameters in the CF and CF-CA populations increased to $8.1\ \mu\text{m}$ and $8.5\ \mu\text{m}$, respectively (Figure 11a). Frequency of occurrences of nonspherical vesicles was also observed. All together, the nonspherical were up to three times more likely to appear in CF and CF-CA exposed populations than in the C population (Figure 11b). The differing occurrence of pearled vesicles was especially noticeable (Figure 11c). In the CF-CA population, their occurrences were ten times greater than the occurrences in the C population.

4 Experiments and results

The MRF image segmentation model was used to detect and segment numerous giant unilamellar vesicles from synthesized images, micrographs, and mosaics from an actual experiment. The results of this segmentation are the first step towards an automated shape analysis of populations of vesicles. As described elsewhere (Zupanc et al., 2011), populations of vesicles were exposed to nanoparticles and shape transformations of the vesicle membranes were observed by recording micrographs of lipid vesicles before and after incubation with nanoparticles. Subsequently, the shapes of lipid vesicles were manually segmented from the micrographs and quantified. In this paper, we propose an MRF image segmentation model allowing automatic segmentation of multiple vesicles from micrographs. To improve the

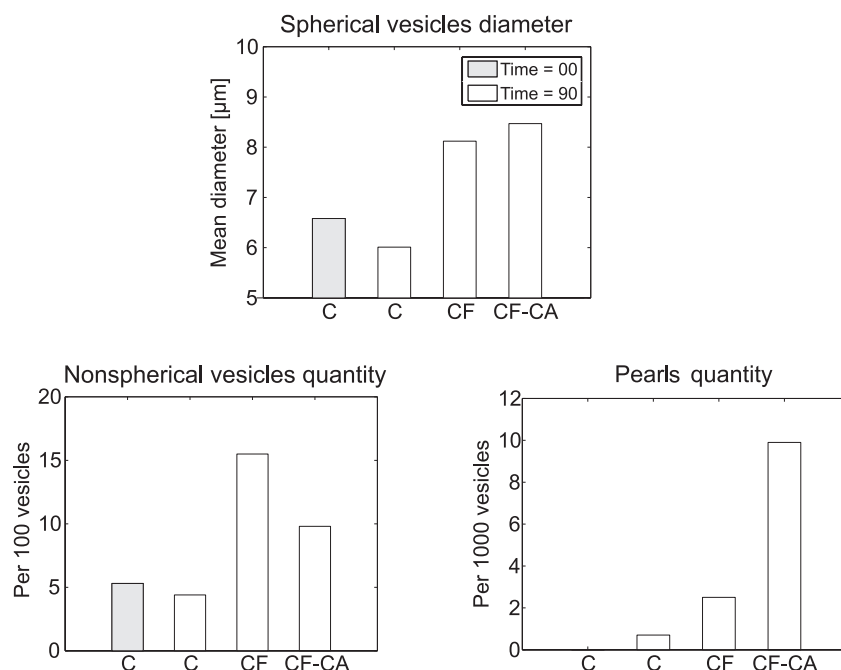


FIGURE 11. Mean diameter size of spherical vesicles for each experimental population (above), number of nonspherical vesicles per 100 vesicles (left), and number of pearled vesicles per 1000 vesicles (right).

separation of the vesicles from the background, we classify the micrograph pixels into three classes, termed: vesicle, halo and background. As intensity alone does not carry enough information to separate the regions, we adapted the neighborhood interactions model of the MRF to incorporate information about proximity of the pixels to each class. Such addition improves the MRF image segmentation model so that it is able to classify a majority of pixels which are surrounded by the pixels labeled as a halo, as the vesicle insides, which was not possible before. When using the original MRF image segmentation model, vesicles tended to be filled only partly. This problem is corrected with our adaptation and the proposed MRF2 model segments the vesicles with improved accuracy.

The proposed MRF2 segmentation model was tested on actual micrographs and its accuracy compared to accuracy of the MRF model without adaptation. Pixel classification error for the vesicles was 12% without and 4% with our adaptation. The modified MRF model also gained greater classification accuracy on synthetic noisy and blurred images. In the comparison with the manual segmentation on an actual experiment with thousands of vesicles, the proposed segmentation requires eightfold less time of an operator, allowing more experiments to be conducted and analyzed in less time.

The MRF2 segmentation model was also tested on an experiment with vesicles and Cobalt-ferrite nanoparticles. After 90 minutes of incubation, the nanoparticle exposed vesicles on average had a larger (8.5 μm) diameter than the unexposed ones (6 μm). Besides the diameter of the spherical we also observed nonspherical vesicles, which were more likely to appear in the exposed populations, especially the pearled vesicles, whose occurrence was ten times greater than in the control. This way, we show the applicability of the method for distinguishing vesicle populations (quantities, sizes) in experiments where vesicle changes are observed not on isolated vesicles but on large vesicle quantities instead.

In the future, this image segmentation model will be used to segment vesicles in multiple experiments regarding shape changes of vesicles due to variety of conditions including drugs, temperature, electric field, and nanoparticles. Also, the algorithms will be made available on the web for other lipid vesicle research groups to use in their experiments. To conclude, the proposed automatic segmentation method, in seconds of computer time, replaces hours of manual segmentation by experts, and offers a convenient and fast procedure to analyze populations of lipid vesicles.

Declaration of interest

The authors report no conflict of interest. The authors alone are responsible for the content and writing of the article.

References

- Alomari RS, Kompalli S, Chaudhary V. (2008). Segmentation of the liver from abdominal CT using Markov random field model and GVF snakes. *Proc. Int. Conf. on Complex, Intel. and Software Intensive Sys.*, 293-298.
- Barauskas J, Cervin C, Jankunec M, Spandyreva M, Ribokaite K, Tiberg F, Johnsson M. (2010). Interactions of lipid-based liquid crystalline nanoparticles with model and cell membranes. *Int. J. Pharmaceutics*, 391(1-2), 284-291.
- Besag J. (1986). On the statistical analysis of dirty pictures. *Journal of the Royal Statistical Society, Series B*, 48:259-302.
- Drobne D, Kralj-Iglic V. (2009). Lipid membranes as tools in nanotoxicity studies. In: *Advances in planar lipid bilayers and liposomes*. Amsterdam; Elsevier: Academic Press, 10:121-134.
- Geman S, Geman D. (1984). Stochastic relaxation, Gibbs distributions, and the Bayesian restoration of images. *IEEE Transactions on Pattern Analysis and Machine Intelligence*, 6:721-741.
- Gruhn T, Franke T, Dimova R, Lipowsky R. (2007). Novel method for measuring the adhesion energy of vesicles. *Langmuir*, 23(10):5423-5429.
- Held K, Kops R, Krause BJ, Wells WM, Kikinis R, Mueller-Gaertner HW. (1997). Markov random field segmentation of brain MR images. *IEEE Transactions on Medical Imaging*, 16(6):878-886.
- Hong S, Leroueil PR, Janus EK, Peters JL, Kober MM, Islam MT, Orr BG, Baker JR, Banaszak Holl MM. (2006). Interaction of polycationic polymers with supported lipid bilayers and cells: nanoscale hole formation and enhanced membrane permeability. *Bioconjug Chem.*, 17(3):728-34.
- Imparato A, Shillcock JC, Lipowsky R. (2005). Shape fluctuations and elastic properties of two-component bilayer membranes. *Europhys. Letters*, 69(4):650-656.
- Kato Z, Pong TC. (2006). A Markov random field image segmentation model for color textured images. *Image and Vision Computing*, 24:1103-1114.
- Li S. (2009). *Random Field Models in Image Analysis*. Computer Science Workbench 3rd ed., 22:362.
- Liu JZ, Hopfinger AJ. (2008). Identification of possible sources of nanotoxicity from carbon nanotubes inserted into membrane bilayers using membrane interaction quantitative structure-activity relationship analysis. *Chem. Res. Toxicol.*, 21(2):459-466.
- Leirer CT, Wunderlich B, Wixforth A, Schneider MF. (2009). Thermodynamic relaxation drives expulsion in giant unilamellar vesicles. *Physical Biology*, 6(1):016011-4.
- Pecreaux J, Dobreiner HG. (2004). Refined contour analysis of giant unilamellar vesicles. *European Physical Journal E*, 13(3):277-290.
- Peterlin P, Jaklic G, Pisanski T. (2009). Determining membrane permeability of giant phospholipid vesicles from a series of videomicroscopy images. *Measurement Science Technology*, 20(5).
- Usenik P, Vrtovec T, Pernus F, Likar B. (2010). Automated Tracking of Vesicles in Phase Contrast Microscopy Images. 2010 Int. Conf. Pattern Recognition, Turkey 2010.
- Valant J, Drobne D, Sepcic K, Jemec A, Kogej K, Kostanjsek R. (2009). Hazardous potential of manufactured nanoparticles identified by in vivo assay. *J. Hazard. Material.*, 171(1-3):160-165.
- Zupanc J, Valant J, Drobne D, Kralj-Iglic V, Iglic A. (2010a). A new approach to analyse effects of nanoparticles on lipid vesicles. *Int. J. Biomedical Nanoscience and Nanotechnology*, 1(1):34-51.
- Zupanc J, Bas E, Erdogmus D. (2010b). Analysis of Lipid Vesicle Populations from Microscopy Video Sequences, 32nd Annual International Conference of the IEEE EMBS.
- Zupanc J, Dobnikar A, Drobne D, Valant J, Erdogmus D, Bas E. (2011). Biological reactivity of nanoparticles: mosaics from optical microscopy videos of giant lipid vesicles, *Journal of Biomedical Optics*, 16(2):0260031-10.